# Classification of Power-line Insulator Condition using Local Binary Patterns with Support Vector Machines

Usiholo Iruansi, Jules R. Tapamo, and Innocent E. Davidson

*Abstract*—**Damaged insulators may affect the mechanical and electrical performance of an electric power grid, which can lead to the flow of leakage currents through the line supports. This increases electrical losses and voltage drop in the power grid. It also poses a risk to human safety. Thus, it is crucial to monitor and inspect the condition of insulators to detect degradation or damage. However, the traditional method of inspection is inadequate in meeting the growth and development of the present electric power grid. Hence an automated system such as the computer vision method is presently being explored as a means to resolve this crisis safely, speedily and accurately. This paper presents a method that distinguishes between defectuous and non-defectuous power-line insulators. Active Contour model is applied for insulator segmentation in order to determine insulator region of interest. Local binary pattern is used for feature extraction from the insulator region of interest which is then fed to the support vector machine classifier for classification. An accuracy of 94.1% was achieved when morphological operation is used in combination with active contour model for segmentation based on the ground-truths. In addition, local binary patterns feature extraction method outperformed gray level co-occurrence matrix when used with support vector machines.**

*Index Terms*—**Active Contour Model, Local Binary Patterns, Power-line Insulator, Support Vector Machines.**

## I. Introduction

Insulators in the electric power grid are materials used to support electrical conductors, while preventing electric current from flowing across them. Insulators are produced from different kinds of materials namely polymer, glass and porcelain. This study is based on polymeric insulators which have a repetitive structure and distinctive circular shape. In the electric power grid, the breakdown caused by insulator defect has a major effect on the transmission and distribution of electricity. Such effects include voltage drop, leakage currents, and electrical losses to the power grid [1], [2]. Hence, there is a need for early detection of insulator defects in order to reduce outages and optimize the performance of the power system.

Power-line inspection is usually carried out manually, either from the lines or from the ground or air using vehicle or helicopter respectively. When inspection of an insulator is carried out directly from the lines, it endangers the inspector since the lines are alongside the insulators. There is a high potential difference between the lines generating an electric and magnetic field in the region of lines at normal condition and higher in the presence of defects [3]. With the traditional method of inspection, on-site insulator condition is not only expensive and time consuming, but challenging to monitor and inspect long lines spanning long distances with difficult terrain. In aerial surveillance such as the use of helicopter for inspection, a trained inspector inside the helicopter is flown around the transmission lines and uses a camera to track and acquire images of the power grid components for further analysis. This method is tedious, expensive and dangerous to the pilot and the trained inspectors when the helicopter is too close to the structures and components of the power grid. The constant vibration and translational movement of the helicopter can affect the sight control of camera and as a result leads to image blurring [3], [4]. Thus an automated system is used to carefully detect the condition of power-line components such as the insulators. Unmanned Aerial Vehicle (UAV) are also employed for power-lines inspection. The UAV employs the principle of the helicopter because of its ability to fly around power-lines. The problem with the UAVs are similar to the helicopter means of inspection, such as proximity and position control. Another approach to power grid inspection is the use of a robot which can move along the lines with its design to overcome barriers on the lines. The main advantage of the robot is its proximity to object of interest and its low vibration, which increases the inspection accuracy and the quality of image acquisition respectively. Therefore, a complete automation system requires embedding computer vision into the robot. Computer vision method has been recognized as a method for monitoring the condition of insulator safely, speedily and accurately. Image processing and computer vision methods are less expensive because of the current technological development in the field of digital imaging and the availability of inexpensive cameras. Therefore, images captured with digital cameras along the power-lines can be sent to the control room for further analysis.

Insulators are a part of the electric power delivery system. To assess the condition of an insulator, it is first extracted from the context. This involves image segmentation using Active Contour Model (ACM) Insulators are a part of the electric power delivery system. To assess the condition of an insulator, it is first extracted from the context. This involves image segmentation using Active Contour Model (ACM) [5] in order to identify the region of interest. Thereafter, features

Manuscript received July 18, 2017; revised October 29, 2017; revised February 03, 2018. This work was supported by the Eskom Power Plant Engineering Institute (EPPEI) Specialization Centre in High Voltage Direct Current (HVDC) Engineering, at the University of KwaZulu-Natal (UKZN), Durban, South Africa.

U. Iruansi is with School of Engineering, University of KwaZulu-Natal, Durban, South Africa e-mail: uiruansi@gmail.com.

J.R. Tapamo is with School of Engineering, University of KwaZulu-Natal, Durban, South Africa e-mail: tapamoj@ukzn.ac.za.

I.E. Davidson is with the Department of Electrical Power Engineering, Durban University of Technology, Durban, South Africa e-mail: innocentd@dut.ac.za.

characterizing the condition of the insulator are considered and are extracted using Local Binary Pattern (LBP) [6] and fed into a Support Vector Machines (SVM) [7] to determine the condition of the insulator.

The paper is organized as follows. Section II discusses previous related work. Section III presents the the proposed method. Section IV validates the proposed method. The paper is concluded in section V.

## II. Related Work

Presently, there are research studies on power grid monitoring and inspection using infra-red and ultraviolet methods [1]. This paper focuses on texture features using image processing and computer vision, where there are scarcely any previous studies.

Insulator fault detection was proposed by Gu et al. [8], but the fault detected is ice or snow coverage on an insulator. It assumes the snow is only gathered along the side or on top of the insulator caps. The fault is said to change the size and edges or boundaries of the insulator cap which is said to be fixed and known. However, this method is based on edge detector and the comparison of the intensities of each extra regions covered by snow or ice with the shell and the background. Comparison of intensity is not robust and for faults such as cracks or broken parts in an insulator, extra regions may not be detected. For instance, an insulator cap with a crack or hole at the centre of the insulator cap may not change the insulator cap size, thereby limiting this method considerably.

For insulator fault detection, Mei et al. [9] and Ge et al. [10] proposed insulator dirt detection for high resolution images. Both methods employed colour model for dirt detection. Colour model is not a robust method for cracks and broken parts. The images in their study were captured at a very close range showing just a single cap of an insulator. In this study, the images show the complete insulator.

A simple method is proposed by Zhang et al. [11], that uses colour thresholding for insulator recognition. This method is not robust because it needs a well adjusted threshold parameter which is a limitation.

Murthy and colleagues in [12] and [13], used Discrete Wavelet Transform (DWT) for feature extraction with SVM and Hidden Markov Model (HMM) for classification respectively. Both methods produced credible results. HMM outperformed SVM. Reddy et al. [14], [15] used Discrete Orthogonal Stockwell Transform (DOST) for feature extraction and Adaptive neuro-fuzzy inference system (ANFIS) and support vector machines (SVM) classification respectively. DOST with SVM outperformed DOST with ANFIS [14], DOST with SVM outperformed DWT with SVM, because DOST has an advantage of maintaining the phase properties of Stockwell transform and Fourier transform, Thus retaining the ability to revert to the Fourier domain.

For the detection of insulator missing cap as defect, Zhang et al. [1] used colour thresholding for segmentation; texture feature sequence extraction using grey level co-occurrence matrix (GLCM), thereafter a further splitting of the insulator into ten parts. The method is limited by the choice of the threshold and the static partitioning does not incorporate differently sized insulators or partially visible insulators. GLCM is invariant to rotation and requires one parameter for directional computation. In this paper, the feature extraction method adopted is Local binary patterns (LBP) [6]. It is robust to the effect of illumination which results in monotonic grey-scale changes, rotation invariant and a very efficient texture operator [16]. However, LBP has gained recognition in many applications (see [17] for applications of LBP) because of its computational simplicity and discriminative power. Prasad and Rao [4], used a local binary pattern in combination with histogram Fourier (LBP-HF). In this paper, our research is based on the use of only LBP for feature extraction.

From this review, it is evident that an automated algorithm which is fast, safe and accurate is vital for insulator condition. This paper presents an automated algorithm for classification of defectuous and non-defectuous power-line insulators.

## III. Proposed Method

### A. Pre-processing

In order to reduce noise and improve the quality of images, pre-processing step is required. Colour images in Red, Green and Blue (RGB) representation are converted into grey scale images as in Figure 1. Morphological operation is applied to enhance images.

Insulator images are enhanced using the top-hat filter [18] as shown in Figure 2. This effectively correct uneven illumination on a varying background. It extracts small elements and details from the given insulator. This is the difference between the given insulator image and its opening using a disk shaped structuring element. The top-hat is defined as:

$$T(I) = I - (I \ o \ S) \tag{1}$$

where $I$ is the insulator image in grey-scale, $S$ is the structuring element which is an open disk of radius 10, and $o$ denotes the opening operation which is the dilation of the erosion of a set $M$ by a structuring element $S$, the opening operation is defined as $[M \ o \ S = (M \ominus S) \oplus S]$. The symbols $\ominus$ and $\oplus$ denotes erosion and dilation respectively.

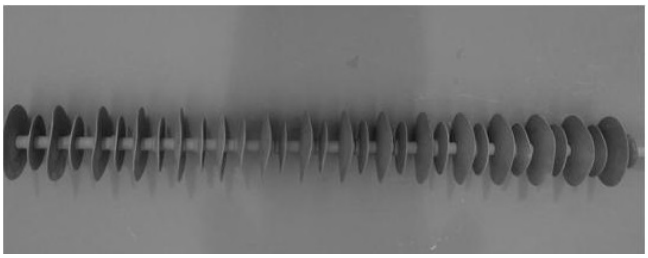

Fig. 1. Greyscale image

The top-hat images obtained are further enhanced by the application of morphological operation [19] known as dilation as shown in Figure 3. The dilation of grey scale images is the replacement of grey level values at any point with the maximum intensity value covered by the structuring element. This is defined as:

$$(I_d \ \oplus \ S)(u,v) = \\ max[I_d(u-u', v-v') - S(u',v')|(u',v') \in D_S \tag{2}$$

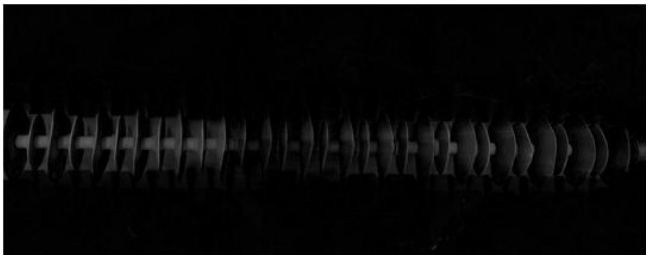

Fig. 2. Top-hat filtering on insulator image in Figure 1

where $I_d$ is the image and $D_S$ is the domain of the structuring element $S$, and $(u, v)$ are pixel coordinates.

In Figure 2, it is observed that the insulator brightness is not uniform along the insulator (not a single connected component). Therefore, morphological dilation is applied to enhance the brightness of the foreground (insulator) or to have a single connected component as shown in Figure 3.

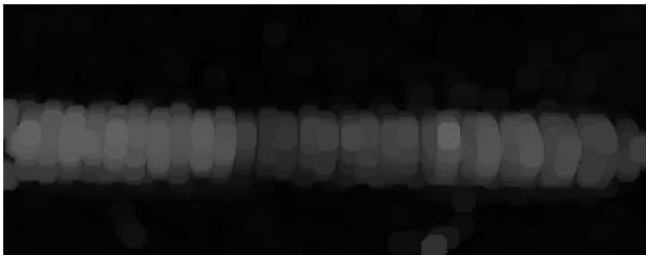

Fig. 3. Grey-scale morphological dilation on insulator image in Figure 2)

The output image of the dilated image is subtracted from the original grey level insulator image for further analysis on insulator segmentation as in Figure 4. The subtracted image is defined as:

$$I_s = I - I_d \tag{3}$$

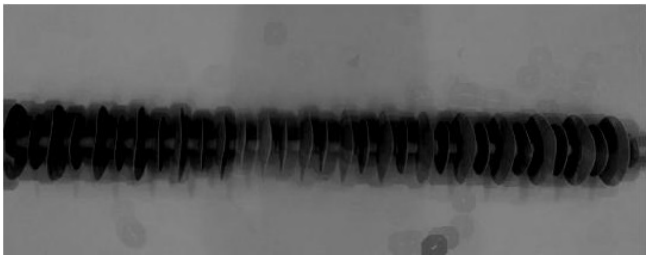

Fig. 4. Subtraction of dilated image from the original grey-scale image

### *B. Insulator Segmentation and Region of Interest Extraction*

*1) Insulator Segmentation:* Considering the properties of an insulator which is a single connected component that has a distinct repetitive circular sheds around its sheath, the region-based is therefore required for insulator segmentation since uniformity of within sub-region is of main interest [2]. Active Contour Model (ACM) has been extensively used in image segmentation such as [2], [5], [20], [21], [22], [23] with promising results. Therefore, region-based ACM without edges is chosen in this paper based on [2] and [5].

ACM is based on Energy function expressed in-terms of level set function $\varphi$ defined as:

$$\begin{aligned} E(k_1, k_2, \varphi) = & \\ & \lambda_1 \int_\Omega (I - k_1)^2 H(\varphi) dx \\ & + \lambda_2 \int_\Omega (I - k_2)^2 (1 - H(\varphi) dx \\ & + \mu \int_\Omega | \bigtriangledown H(\varphi)| dx \end{aligned} \tag{4}$$

where $\varphi$ is the level set function, $\Omega$ is an open bounded region with foreground $\Omega_1$, background $\Omega_2$, $\lambda_1$, $\lambda_2$ and $\mu$ are fixed parameters with their settings as $\lambda_1 = \lambda_2 = 1$ and $\mu = 1$. The Heaviside step function $H$, and mean intensities $k_1$ and $k_2$ are defined as:

$$k_1(\varphi) = \frac{\int_\Omega I(u) H(\varphi(u)) du}{\int_\Omega H(\varphi(u)) du} \tag{5}$$

$$k_2(\varphi) = \frac{\int_\Omega I(u)(1 - H(\varphi(u))) du}{\int_\Omega (1 - H(\varphi(u))) du} \tag{6}$$

$$H(\varphi) = \begin{cases} 1, & \text{if } \varphi \geq 0 \\ 0, & \text{if } \varphi < 0 \end{cases} \tag{7}$$

$$\varphi = \begin{cases} 0, & \text{if } \varphi \text{ is at the boundary of the curve} \\ > 0, & \text{if } \varphi \text{ is inside the curve} \\ < 0, & \text{if } \varphi \text{ is outside the curve} \end{cases} \tag{8}$$

From equation (4), the first term is a measure of the variance of the background grey level in regards to pixel intensity in the image, the second term is a measure of the variance of the insulator (foreground) grey level based on the measure of uniformity of pixel intensity in the image and the third term expresses the length of the boundary of the insulator in the image $I$. $H(\varphi)$, is the Heaviside function of the level set function. The Heaviside function determines the insulator image and the background regions in the observed image $I$.

Thus, to segment insulator from an image, equation (4) is minimized with respect to $k_1$, $k_2$ and $\varphi$. With $\varphi$ constant, the mean grey values of $k_1$ and $k_2$ are computed with equation (5) and (6) respectively. Also, with $k_1$ and $k_2$ constant using calculus of variations for equation (4), the gradient decent equation for the evolution of $\varphi$ is derived as:

$$\frac{\partial \varphi}{\partial t} = \delta(\varphi) \left[ \mu \nabla . \left( \frac{\nabla \varphi}{|\nabla \varphi|} \right) - \lambda_1 (I - k_1)^2 + \lambda_2 (I - k_2)^2 \right] \tag{9}$$

where $\nabla.(\nabla\varphi/|\nabla\varphi|)$ is the curvature of the curve, that provides smoothing constraints during curve evolution thereby minimizing the total curvature of the contour. The Dirac measure is applied in order to work very close to the minimization problem. The Dirac measure is defined as:

$$\delta(\varphi) = \frac{d}{d\varphi} H(\varphi) \tag{10}$$

Figure 5 shows the initial curve $\varphi$ in an image $I$, where $k_1$ and $k_2$ are the average intensities values inside and outside $\varphi$ respectively and the length of the edge contour is evolved in order to fit the boundary of the insulator such as in Figure 6. At this point the curve becomes stationary and the interclass variance is minimized and the segmented image is achieved as shown in Figure 7.

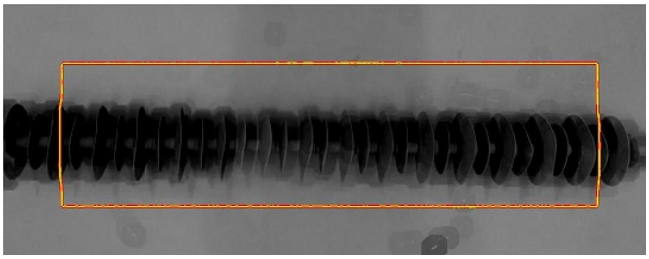

Fig. 5. Initial curve $C$ of ACM implementation on Figure 4. (Best viewed in colour)

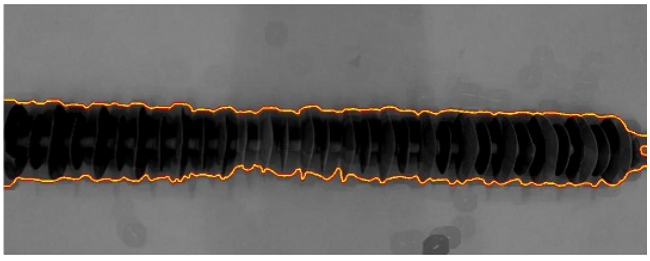

Fig. 6. ACM curve on insulator boundary. (Best viewed in colour)

Fig. 7. Segmented image of Figure 6

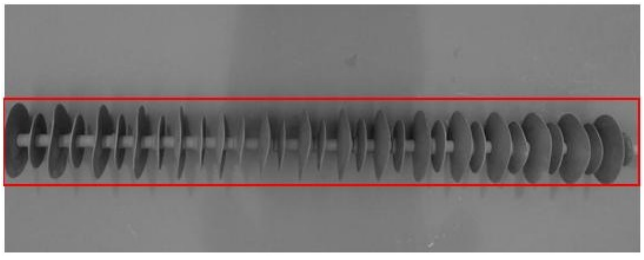

Fig. 8. Insulator ROI, using the coordinates extracted from the segmented insulator in Figure 7 to place a bounding box on insulator in Figure 1. (Best viewed in colour)

*2) Region of Interest:* Insulator region of interest (ROI) is extracted by first obtaining the coordinates and size of the foreground pixels (insulator) from the segmented image, then with same size of segmented image and the original grey scale image, the coordinates and size from the segmented

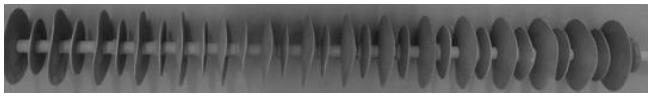

Fig. 9. Extracted insulator ROI from Figure 8

image is mapped into the original grey scale image for placing a minimum bounding box over the entire insulator, thereafter extraction of the insulator ROI.

*3) Algorithm of Insulator Segmentation and Region of Interest Extraction:* Algorithm 1 gives the steps for insulator segmentation and extraction of insulator ROI.

**Algorithm 1** Insulator Segmentation and ROI

**Require:** $I$ ▷ Source Image
**Ensure:** $E$ ▷ Extracted Image of Insulator ROI
1: Convert the original colour image $I$ into grey scale and Save result as $g$
2: Define a structuring element $s$ of disk with radius 10
3: Apply Equation 1 on $g$ and Save result as $T$
4: Apply Equation 2 on $T$ and Save result as $T_d$
5: Apply Equation 3 and Save result as $I_s$
6: Initialize a level set function $\varphi$
7: **for** n = 1 to maximum value of n **do**
8: Compute $k_1(\varphi)$ and $k_2(\varphi)$ using equation 5 and 6 respectively
9: Compute $\varphi^{n+1}$ by the discretization and linearization of equation 9
10: Check whether curve is stationary
11: **if** curve is stationary **then**
12: Escape from the for loop
13: **end if**
14: **end for**
15: Save segmented image as $sIm$
16: Extract coordinates of the ROI from $sIm$
17: Map the coordinates from $sIm$ on $g$
18: Extract insulator ROI from $g$ and save as $E$
19: Partition $E$ and save into a folder $F$ (training set)
**20: End**

### C. Feature Extraction using Local Binary Patterns

Local binary pattern is a feature extraction method that is non-parametric. It is grey-scale implementation, invariant to rotation and describes the spatial structure of the local texture of an image [24]. In recent years, its application has increased in image processing and computer vision due to its simplicity in computation and changes to tolerance in monotonic illumination [17]. LBP has been used in many applications, such as defect detection [25], fingerprint liveness detection[26], [27], visual inspection [28] and biometrics [29].

The principle of the original version of LBP [30] is to produce labels by using the middle value as a threshold for converting its neighbouring pixels into binary numbers. If pixels equal or greater than the threshold value, it is referred to as one. Pixels less than the threshold value are referred to as zero. Then, a histogram is generated which is used as a texture descriptor. The disadvantage of the initial form of the LBP, is that computation of features in a local region of $3 \times 3$ fail to acquire the most important features of textures in a large structure. Thus, the initial LBP was modified to use neighbourhood of various sizes [6]. The extended LBP adopts the circular neighbourhoods and interpolates values bi-linearly at pixels coordinates that are non-integer. This allows for any radius and number of pixels in the neighbourhood.

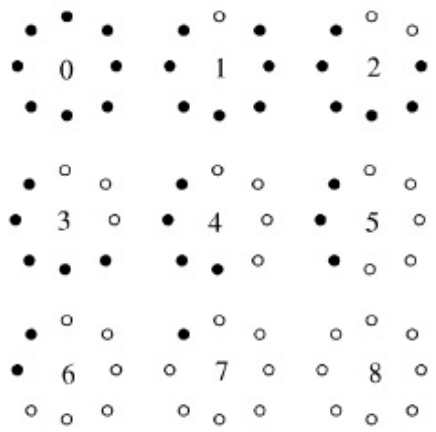


Fig. 10. Uniform patterns with number of transition less or equal to 2 ($\leq 2$) and the values inside the patterns correspond to their unique codes. The white and black circles denotes bit values of 1 and 0 in the 8-bit output of the operator [6].

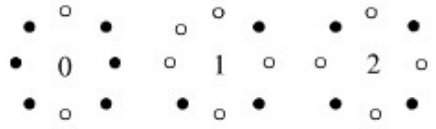


Fig. 11. Non-uniform patterns with number of transition greater than 2 ($> 2$).

An additional development to the initial LBP is to use a fundamental pattern called "Uniform" since they have a circular structure that are uniform and have very few spatial transition [6]. Figure 10 describes the uniform pattern which functions as a template for micro-structures such as bright spot (0), edges of varying negative and positive curvature ($1-7$) and flat area or dark spots (8). Figure 11 shows a non-uniform pattern. The Local binary pattern is defined as a uniform pattern if the bitwise change in state from $0-$to$-1$ or $1-$to$-0$ of the binary bit pattern which has a maximum of two-bitwise change in state when the pattern of the bit is cross over circularly as shown in Figure 10. For example, the pattern 00000001 and 00010000 have 1-transitions and 2-transition respectively for uniform patterns. Thus the patterns contains a maximum of two, $0-$to$-1$ and $1-$to$-0$ transitions. The pattern 10000100 is considered a non-uniform pattern since it has a 3-bitwise change of state (3-transition).

In this research investigation the uniform patterns are used, because most natural images contains uniform pattern [6], reduction in the length of the feature vector, invariant to rotation and have produced better recognition in many computer vision applications [31].

To compute the LBP histogram using uniform patterns, the LBP histogram accumulates all non-uniform patterns greater than $2-$bitwise change of state into bin 0, and every other bins of uniform patterns are accumulated in a dedicated bin as shown in Table I for simplicity using $(8, 1)$ neighbourhood, it gives a total of 256 patterns, 58 of which are uniform, which gives 59 different labels (see Table I) [6]. A histogram is computed over all cells based on the frequency of occurrence of each number and thereafter normalized. The histogram of all cells concatenated, which gives the feature vector that will be fed into the classifier.

$$H_k = \sum_{q,r} I[f(q,r) = k], k = 0, ..., n-1 \quad (11)$$

where, $f(q, r)$ is the LBP labelled image, $n$ denotes the number of different labels generated with the LBP operator and $I(B)$ is defined as

$$I\{B\} = \begin{cases} 1, \text{ if } B \; is \; true \\ 0, \text{ if } B \; is \; false \end{cases}$$

TABLE I
COMPUTATION OF UNIFORM LBP LABELS AND THE FINAL $59-$BIN HISTOGRAM, WITH "XX" REPRESENTING THE NON-UNIFORM PATTERNS

| Decimal | Binary | No of Transition | Histogram |
|---|---|---|---|
| xx | xx | $> 2$ | 0 |
| 0 | 00000000 | 0 | 1 |
| 1 | 00000001 | 1 | 2 |
| 2 | 00000010 | 2 | 3 |
| . | . | . | . |
| . | . | . | . |
| . | . | . | . |
| 254 | 11111110 | 1 | 57 |
| 255 | 11111111 | 0 | 58 |

### D. Classification

*1) Classification using Support Vector Machines:* The extracted feature vectors are fed into a SVM classifier [7] in order to classify insulators into defectuous and non-defectuous. SVM is a supervised learning technique [26] used for regression and classification. A very useful property of the SVM is that it minimizes the error of unknown test samples for classification by constructing an optimal hyperplane. When SVM is used for training, the optimal hyperplane is defined by the one with the maximum distance from the nearest training pattern, called support vectors. Apparently, it can be deduced that the hyperplane with the longest distance to the neighbouring data points of both classes has the best separation. The generalization error of the classifier increases as the margin or distance between these parallel hyperplanes increases. For two classes that are not separable, the optimal hyperplane maximizes the margin and minimizes the misclassification errors. The balance achieved between the misclassification error and margin is regulated by a positive constant that has to be selected earlier.

Thus, for a set of $Z$ training samples $(v_i, w_i)$ where $v_i \in R^N$ and $w_i$ is the label $(w_i \in (-1, 1))$, a SVM classifier determines the optimal hyperplane. The discriminant hyperplane is defined as:

$$f(v) = \sum_{i=1}^{Z} \alpha_i w_i . k(v, v_i) + b \quad (12)$$

where $b$ is a scalar (bias), $\alpha_i$ is formulated with constraints, the sign of $f(v)$ defines the class membership of $v$ and $k(v, v_i)$ is a kernel function. In this research work, a non-linear kernel function known as radial basis function (rbf) with a sigma value of 1 is used. The rbf kernel is defined as $k(v, v_i) = exp(-\gamma||v - v_i||^2)$. $\gamma$ is the spread of Gaussian cluster.

*2) Classification using K-Nearest Neighbour:* Typically, KNN is used to train a set of feature vectors or attribute vectors with a given corresponding class label in order to predict a class of an unknown instance $x$. An instance $x$ relates to a point in a n-dimensional space and can be represented by an attribute vector $[v_1(x), v_2(x), ..., v_n(x)]$, where $n$ is the number of attributes. In our case, KNN uses the Euclidean distance to measure the distance between instance $x_i$ and $x_j$. The Euclidean distance is defined in [32], [33], [34] as:

$$d(x_i, x_j) = \sqrt{\sum_{m=1}^{n} (v_m(x_i) - v_m(x_j))^2} \tag{13}$$

Given a new instance $y$, KNN uses the k-nearest instance in the training set i.e. $x_1, x_2, ..., x_k$, thereby returning the result of classifying $y$ as defined in equation 14.

$$c(y) \leftarrow \arg\max_{c \in C} \sum_{r=1}^{k} \delta(c, c(x_i)) \tag{14}$$

where $c(y)$ is the class of the instance $y$, $k$ is the number of neighbours, $C$ and $c$ represents the class variable and $\delta(c, c(x_i))$ is equal to 1, if $c$ is equal to $c(x_i)$ and 0 otherwise.

### *E. Algorithm for the classification of power-line insulator condition*

Algorithm 2 gives the steps involved in the classification of power-line insulator condition using LBP with SVM.

**Algorithm 2** Classification of a power-line Insulator $Ins$ using a Support Vector Machine, $TSVM$, trained with training set $TrainSet$ of insulators

**Require:** $Ins, TSet$ ▷ $Ins$ is the insulator image, $TSet$ is the training set of insulator images
**Ensure:** $condition$ ▷ condition of the given insulator $Ins$
1: $TSVM$ = **TrainingSVM**($TSet, TSVM$)
2: condition = **SVMclassify**($TSVM, Ins$)
3: **return** $condition$ ▷ condition of the insulator $Ins$

Algorithm 3 trains a Support Vector Machine, $TSVM$, using a set of insulator images.

**Algorithm 3** Training of a Support Vector Machine using a training set, $TSet$ insulators images

1: **procedure** TRAININGSVM($TSet$) ▷ Training set $TSet$
2: **for** each image $T \in TSet$ **do**
3: $M$=**FeatureExtraction**($T$)
4: **Feed** $M$ into $TSVM$ for training
5: **end for**
6: **return** $TSVM$ ▷ $TSVM$ is the Trained classifier
7: **end procedure**

Algorithm 4 computes the feature vectors using the image of an insulator.

**Algorithm 4** Feature extraction from a power-line Insulator image $Ins$ using using Local Binary Pattern

1: **procedure** FEATUREEXTRACTION($Ins$) ▷ image $Ins$
2: **Convert** $Ins$ into grayscale and save it in $g$
3: **Apply** $LBP$ operator on $g$ and save result as $L$
4: **Compute** $LBP$ histogram $H$ from $L$
5: **Calculate** the feature vector $M$ from **H**
6: **return** $M$ ▷ The Feature vector is $M$
7: **end procedure**

## IV. Experimental Results and Discussion

### *A. Dataset*

To the best of our knowledge there is presently no publicly available dataset for insulator studies. Hence, the experiment is based on our own dataset to evaluate the proposed method. The experiment was conducted on polymeric insulator. The dataset contains 600 insulator images of both defectuous and non-defectuous insulators. The training set is made up of 200 defectuous and 200 non-defectuous insulator images (Figure 12). For the training set, a 10-fold cross validation is applied. The test set is made of 200 insulator images with 100 defectuous and 100 non-defectuous insulator images that are not partitioned.

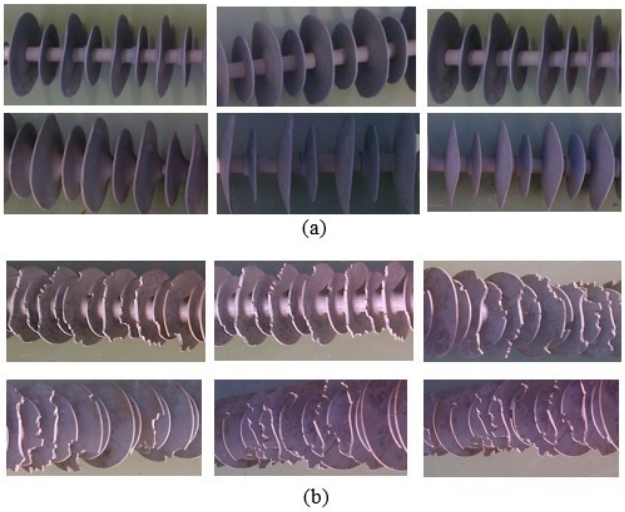


Fig. 12. Dataset of non-defectuous and defectuous insulators.

### *B. Results*

*1) Pre-processing:* Due to noises (such as shadows and illumination) in the captured images during insulator image acquisition, all insulator images were pre-processed before further analysis. Morphological dilation was applied to increase the brightness of the foreground (insulator) in order to have single connected component as shown in Figure 3.

*2) Segmentation:* Figure 13 shows the results of the segmented insulator images. It is observed that the ACM curve fits on the boundary of the insulators in Figure 13(a) and the binarized segmented images are shown in Figure 13(b). In Figure 13, it is observed that some background pixels are inside the insulator (foreground), as a result post-processing was employed to fill up the holes as shown in Figure 14.

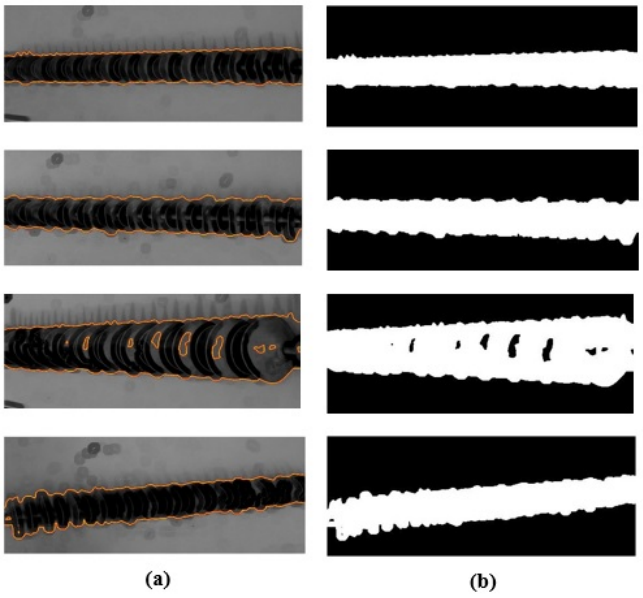


Fig. 13. Some results of (a) implementation of ACM with curve on insulator boundaries and (b) the segmented images. Best viewed in colour.


Fig. 14. Results of post-processing of (a) Figure 13 on row 3 column 2 and (b) row 4 column 2.

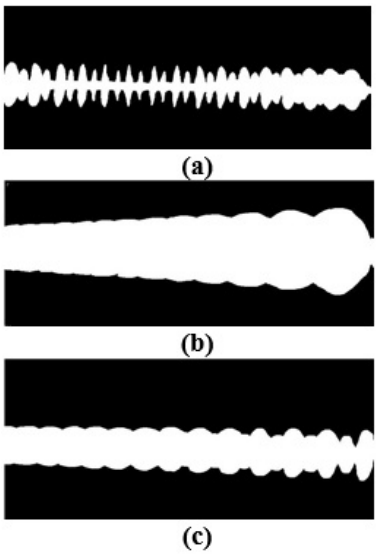


Fig. 15. Some ground-truth images

In order to evaluate the segmentation method, segmented insulator images created by experts were used. Some ground-truth samples are presented in Figure 15. Since interest is on the ROI of the insulator, the minimum bounding box over the insulator is required. Therefore, the ground-truth bounding box over the insulator (foreground) is considered as the relevant object and the bounding box of the proposed segmented insulator region is considered as the selected object. Based on this explanation, a statistical criteria was employed for performance analysis. Precision $(Pr)$, Recall $(Re)$, F1-score $(Fs)$ and Accuracy $(Ac)$ [35], [36] and are defined as

$$Pr(\%) = tp_s/(tp_s + fp_s) \quad (15)$$

$$Re(\%) = tp_s/(tp_s + fn_s) \quad (16)$$

$$Fs(\%) = 2tp_s/(2tp_s + fp_s + fn_s) \quad (17)$$

$$Ac(\%) = (tp_s + tn_s)/(tp_s + tn_s + fp_s + fn_s) \quad (18)$$

where the foreground represents the pixels inside the bounding box or ROI and background represents the pixels outside the ROI in both segmented images and ground-truth images. All images are in binary for computation. True positive $tp_s$ is the foreground in the segmented image that overlaps the foreground in the ground-truth image. True negative $tn_s$ is the background in the segmented image that truly overlaps the background in the ground-truth image. False positive $fp_s$ is the foreground in the segmented image that are detected as background in the ground-truth image. False negative $fn_s$ is the background in the segmented image that are defined as the foreground in the ground-truth image. Table II shows the result of the performance analysis.

TABLE II
PERFORMANCE ANALYSIS

| Method | Precision | Recall | F1-Score | Accuracy |
|---|---|---|---|---|
| Proposed method | 87.6% | 99.6% | 93.0% | 94.1% |

The extracted coordinate, length and width of the insulator (foreground) image in the segmented image is used to define the insulator ROI in the grey-scale image as shown in Figure 16 and 17. The red bounding box (denoted with a solid triangle) represents the insulator ROI using the proposed method of segmentation and green bounding box (denoted with a solid rectangle) represents the ground-truth. It is observed in Figure 16 that both the proposed method of segmentation and the ground-truth overlap each other while in Figure 17 the area of the proposed method is more than the ground-truth. This means that there is an under-segmentation as a result of the strong edge boundary from the insulator shadow. This reduces the performance of segmentation. Furthermore, the extracted coordinate, length and width are used to extract the insulator ROI as shown in Figure 18 from the original grey-scale image.

*3) Feature Extraction:* Due to the length of each insulator, it was difficult to capture some smaller regions that are defectuous, therefore each insulator image is partitioned into smaller segment for enhanced classification performance. Figure 19 shows an insulator image that has been partitioned.

The performance of the proposed model was compared with the GLCM feature extraction implemented in [1]. GLCM is a texture feature extraction model. The most

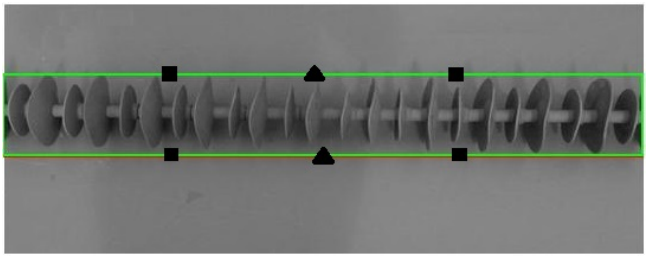

Fig. 16. Minimum bounding box identified as ROI. The red bounding box (denoted with a solid triangle) represents proposed method of segmentation and green bounding box (denoted with a solid rectangle) represents ground-truth. Best viewed in colour

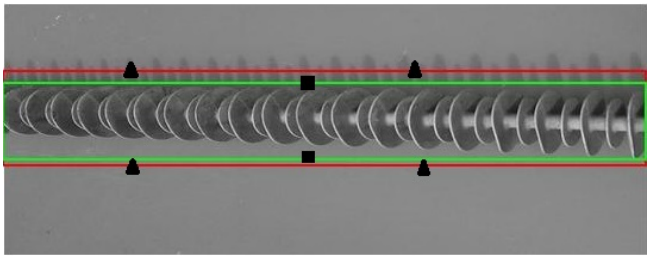

Fig. 17. The red bounding box (denoted with a solid triangle) represents the proposed method of the segmentation and green bounding box (denoted with a solid rectangle) represents the ground-truth. Best viewed in colour

Fig. 18. ROI extracted from Figure 1 using the bounding box coordinates obtained from the insulator segmentation.

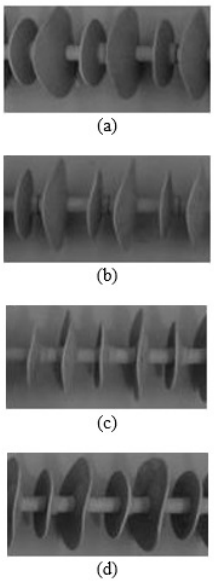


Fig. 19. Insulator partitioning of Figure 18.

popular used GLCM features (also known as Haralick features) are: angular second moment (energy), contrast, sum of squares (variance), correlation, inverse difference moment (homogeneity), sum variance, sum average, entropy, sum entropy, difference variance, difference entropy, maximum correlation coefficient, information measure of correlation 1, and information measure of correlation 2. Computation of these features are described in [37]. Features with better performance are always selected from the fourteen Haralick features when carrying out an experiment. In [1], seven textural features were used. It computes the second order statistics related to image properties by considering the spatial relationship of pixels. It denotes how often different combinations of grey levels co-exist in an image. It is created by calculating how often a pixel with the intensity value $i$ occurs in a specific spatial relationship to a pixel with the intensity value $j$ in an image [38]. Given an image $I$ with $G$ grey levels, distance $d$ and angle $\theta$, for a grey level co-occurrence matrix $[P_{d,\theta}(i,j)]_{0\leq i,j\leq G-1}$. The computation of Haralick features is done using a normalized GLCM. The $(i,j)th$ normalized entry, $[P_{d,\theta}(i,j)]$, of $[P_{d,\theta}(i,j)]$ is defined as [39]:

$$P_{d,\theta}(i,j) = \frac{P_{d,\theta}(i,j)}{\parallel P_{d,\theta} \parallel} \tag{19}$$

where $\parallel P_{d,\theta} \parallel = \sum_{i=0}^{G-1} \sum_{j=0}^{G-1} P(i,j)$.

*4) Classification:* Tables III and X show the 10-fold Cross-Validation (CV) and the condition of insulator test set images for the proposed model and GLCM [1].

The performance analysis of the proposed method was measured using equation (18). The accuracy of the proposed model and that of GLCM [1] in combination with either SVM or KNN with the testing set images are shown in Table XI. Hence, a better performance is obtained when LBP is used as a feature extraction method in combination with either of the classifiers over GLCM.

TABLE III
CONFUSION MATRIX FOR THE CV USING LBP WITH SVM

| | Defectuous | Non-defectuous |
|---|---|---|
| Defectuous | 200 | 0 |
| Non-defectuous | 0 | 200 |

TABLE IV
CONFUSION MATRIX FOR THE CV USING GLCM [1] WITH SVM

| | Defectuous | Non-defectuous |
|---|---|---|
| Defectuous | 188 | 12 |
| Non-defectuous | 9 | 191 |

TABLE V
CONFUSION MATRIX OF THE TEST SET USING LBP WITH SVM

| | Defectuous | Non-defectuous |
|---|---|---|
| Defectuous | 94 | 6 |
| Non-defectuous | 23 | 77 |

TABLE VI
CONFUSION MATRIX OF THE TEST SET USING GLCM [1] WITH SVM

| | Defectuous | Non-defectuous |
|---|---|---|
| Defectuous | 87 | 13 |
| Non-defectuous | 27 | 73 |

In order to validate the accuracy of the methods, the McNemar's test introduced by Quinn McNemar in 1947 is used. The McNemar's test is a statistical test used on paired (matched) data on a dichotomous item. Considering

TABLE VII
CONFUSION MATRIX FOR THE CROSS-VALIDATION USING LBP WITH KNN

| | Defectuous | Non-defectuous |
|---|---|---|
| Defectuous | 200 | 0 |
| Non-defectuous | 0 | 200 |

TABLE VIII
CONFUSION MATRIX OF THE TEST SET USING LBP WITH KNN

| | Defectuous | Non-defectuous |
|---|---|---|
| Defectuous | 94 | 6 |
| Non-defectuous | 24 | 76 |

TABLE IX
CONFUSION MATRIX FOR THE CROSS-VALIDATION USING GLCM WITH KNN

| | Defectuous | Non-defectuous |
|---|---|---|
| Defectuous | 190 | 10 |
| Non-defectuous | 10 | 190 |

TABLE X
CONFUSION MATRIX OF THE TEST SET USING GLCM WITH KNN

| | Defectuous | Non-defectuous |
|---|---|---|
| Defectuous | 88 | 12 |
| Non-defectuous | 30 | 70 |

TABLE XI
ACCURACY OF GLCM AND LBP USING SVM AND KNN CLASSIFIERS

| | 10-fold validation ACC (%) | Testing ACC (%) |
|---|---|---|
| GLCM+SVM | 94.8% | 80.0% |
| GLCM+KNN | 95% | 79.0% |
| LBP+SVM | 100% | 85.5% |
| LBP+KNN | 100% | 85.0% |

the feature extraction methods with SVM classifier, let $A$ be the combination of GLCM with SVM algorithm and $B$ be the combination of LBP with SVM algorithm. Given the following number of cases, Table XII shows that:

- Number of insulators estimated defectuous for $A$ and defectuous for $B$ = a
- Number of insulators estimated non-defectuous for $A$ and defectuous for $B$ = b
- Number of insulators estimated defectuous for $A$ and non-defectuous for $B$ = c
- Number of insulators estimated non-defectuous for $A$ and non-defectuous for $B$ = d

TABLE XII
CONTINGENCY TABLE

| | | A | |
|---|---|---|---|
| | | Defectuous | Non-defectuous |
| B | Defectuous | a | b |
| | Non-defectuous | c | d |

The McNemar's test uses data from the two discordant entries $b$ and $c$ from Table XII, where $n$ is the total number of matched pairs ($n = a+b+c+d$). The McNemar's test is used to determine whether the null hypothesis $H_o$ is accepted or rejected. The $H_o$ states that there is no significant difference between the two algorithms and alternative hypothesis $H_a$ states that there is a significant difference between both algorithms. The McNemar's test is computed using Equation 20.

$$\chi^2 = \frac{(|b-c|-1)^2}{b+c} \tag{20}$$

where $\chi^2$ is chi-squared distribution with one degree of freedom (DoF).

Therefore, the computed chi-square value ($\chi^2$) using Equation 20 is 13.04. A $P$ value of 0.05 (5%) is used for the significant test. However, if it is greater, then the null hypothesis $H_o$ is rejected. The $P$ value of 0.05 for 1 DoF in the chi-square ($\chi^2$) distribution table is 3.841. Since the computed $\chi^2 > 3.841$, $H_o$ is rejected. Therefore, it means that the accuracy of the two algorithms (A and B) are statistically different.

### C. Discussion

In the classification phase, SVM with radial basis function kernel was used. A Cross Validation (CV) process was performed in order to predict or optimize the model parameter (regularization parameter and kernel width) to fit the training set. A k-fold cross-validation randomly partitions the training set into k-equal sized subset, whereby a single subset was retained as a test set and all other subsets were used as the training set. Then the cross-validation process is repeated based on the number of fold (k) times, with the k subset used once as the validation set. Thereafter averaging the k results of all folds to obtain a single result. The number of fold is varied from 2 to 10 and the accuracy was computed using equation 18. The result is shown in Figure 20.

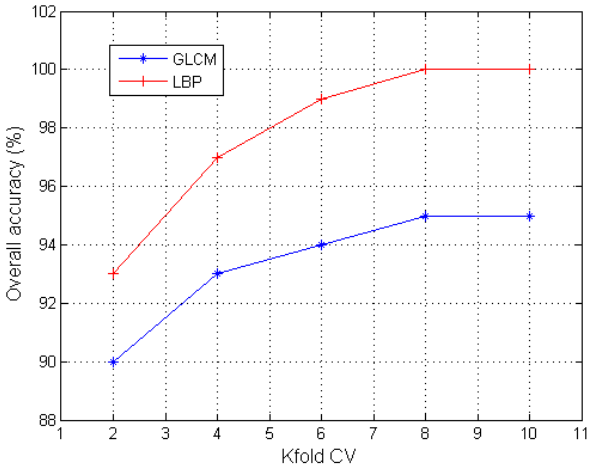


Fig. 20. Accuracy on cross-validation using SVM

In Figure 20, the accuracy of both methods (LBP, GLCM) increases from k = 2 to k = 10. If 5% is considered as the threshold of the error rate (1-accuracy(%)), then it can be stated that a better fitting model to the training set was achieved from k = 8 to 10 for both methods. There was an increase in both methods because of the principle of k-fold CV. For example, at k = 2, it partitions the training set into 2 equal sizes, i.e 50:50, which means it trains with one part of the 50 and test with the other part of 50. For k = 10, it partitions the training set into 10 equal sizes, i.e 20:80, and used the 80 for training while the 20 for testing. Comparing both cases of k = 2 and k = 10, it means that more images will

be used for training for k = 10 than k = 2, as a result having a better chance to identify unknown image. The classifiers performed best for k = 10 and worst for k = 2.

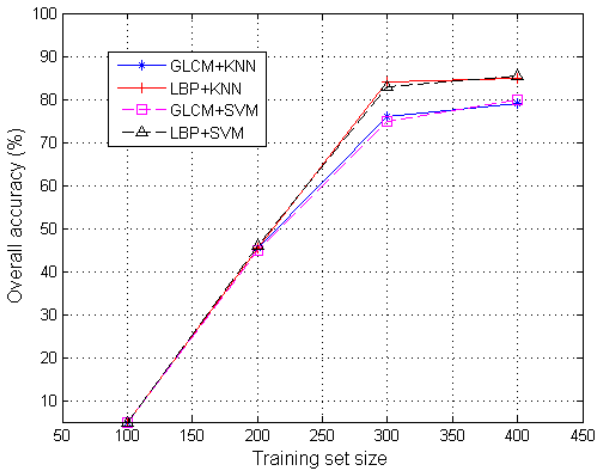


Fig. 21. Accuracy on testing set using SVM and KNN

Figure 21 shows the overall accuracy when the training set was varied from 100, 200, 300, 400, along side the test set from 500, 400, 300, 200 respectively for SVM and KNN classifier using LBP and GLCM as feature extraction methods. Each pair (training set and test set) amount to 600 images in all cases of varying the size of the dataset. The increasing training set size increases the accuracy and decreases the error rate. It can be observed in Figure 21, that there is a sharp rise in the training set when increased from 100 to 300. When, the training set is increase above 300, a gradual increase is noticed. At this point forward, there is a reduced error rate which may stay approximately same within this region and this region is where the model performed best. Both classifiers performed well with a training set above 300 samples (Figure 21), but LBP in combination with SVM has the highest performance (85.5%) compared to others using a training set of 400 samples.

## V. Conclusion

In this paper, classification of power-line insulator condition have been investigated and presented. The segmentation method was evaluated using manually create ground-truth by experts. Also comparison of LBP and GLCM feature extraction method are presented. It is shown that LBP outperformed GLCM with the use of the same classifier. From the experiment, it is evident that the LBP is statistically robust, more stable and less prone to noise.

In future, other methods of feature extraction should be implemented and compared with our proposed method that have been established as a baseline. Consideration of the integration of insulator condition in real-time system should be established.

## Acknowledgment

The authors would like to thank Eskom Power Plant Engineering Institute Specialization Centre in High Voltage Direct Current Engineering, at the University of KwaZulu-Natal, Durban, South Africa.

## References

[1] Z. Xinye, J. An, and F. Chen, "A method of insulator fault detection from airborne images," in *Second WRI Global Congress on Intelligent Systems*, vol. 2. IEEE, 2010, pp. 200–203.

[2] U. Iruansi, J. R. Tapamo, and I. E. Davidson, "An active contour approach to insulator segmentation," in *Proceeding of the 12th IEEE AFRICON International Conference*. IEEE, 2015, pp. 1–5.

[3] J. Katrasnik, F. Pernus, and B. Likar, "A climbing-flying robot for power line inspection," in *Proceedings of the IEEE Conference on Robotics, Automation and Mechatronics*. IEEE, 2008, pp. 95–110.

[4] P. S. Prasad and B. P. Rao, "LBP-HF features and machine learning applied for automated monitoring of insulators for overhead power distribution lines," in *International Conference on Wireless Communications, Signal Processing and Networking (WiSPNET)*. IEEE, 2016, pp. 808–812.

[5] T. F. Chan and L. A. Vese, "Active contours without edges," *IEEE Transactions on image processing*, vol. 10, no. 2, pp. 266–277, 2001.

[6] T. Ojala, M. Pietikainen, and T. Maenpaa, "Multiresolution gray-scale and rotation invariant texture classification with local binary patterns," *IEEE Transactions on Pattern Analysis and Machine Intelligence*, vol. 24, no. 7, pp. 971–987, 2002.

[7] C. Cortes and V. Vapnik, "Support-vector networks," *Machine learning*, vol. 20, no. 3, pp. 273–297, 1995.

[8] I. Y. Gu, U. Sistiaga, S. M. Berlijn, and A. Fahlstrom, "Online detection of snowcoverage and swing angles of electrical insulators on power transmission lines using videos," in *16th IEEE International Conference on Image Processing (ICIP)*. IEEE, 2009, pp. 3249–3252.

[9] X. Mei, T. Lu, X. Wu, and B. Zhang, "Insulator surface dirt image detection technology based on improved watershed algorithm," in *Asia-Pacific Power and Energy Engineering Conference (APPEEC)*. IEEE, 2012, pp. 1–5.

[10] Y. Ge, B. Li, S. Zhao, and C. Pang, "Detection of the insulator dirtiness based on the computer vision," in *China International Conference on Electricity Distribution (CICED 2006)*. IET, 2006, pp. 173–176.

[11] Z. Xinye, J. An, and F. Chen, "A simple method of tempered glass insulator recognition from airborne image," in *International Conference on Optoelectronics and Image Processing (ICOIP)*, vol. 1. IEEE, 2010, pp. 127–130.

[12] V. S. Murthy, K. Tarakanath, D. K. Mohanta, and S. Gupta, "Insulator condition analysis for overhead distribution lines using combined wavelet support vector machine (SVM)," *IEEE Transactions on Dielectrics and Electrical Insulation*, vol. 17, no. 1, pp. 89–99, 2010.

[13] V. S. Murthy, S. Gupta, and D. K. Mohanta, "Digital image processing approach using combined wavelet hidden markov model for well-being analysis of insulators," *IET Image Processing*, vol. 5, no. 2, pp. 171–183, 2011.

[14] M. J. B. Reddy, B. K. Chandra, and D. K. Mohanta, "A DOST based approach for the condition monitoring of 11 kv distribution line insulators," *IEEE Transactions on Dielectrics and Electrical Insulation*, vol. 18, no. 2, pp. 588–595, 2011.

[15] M. J. B. Reddy, D. K. Mohanta, and K. B. Chandra, "Condition monitoring of 11kV distribution system insulators incorporating complex imagery using combined DOST-SVM approach," *IEEE Transactions on Dielectrics and Electrical Insulation*, vol. 20, no. 2, pp. 664–674, 2013.

[16] M. Pietikainen, "Local binary patterns," *Scholarpedia, 5(3):9775*, 2010.

[17] D. Huang, C. Shan, M. Ardabilian, Y. Wang, and L. Chen, "Local binary patterns and its application to facial image analysis: a survey," *IEEE Transactions on Systems, Man, and Cybernetics, Part C (Applications and Reviews)*, vol. 41, no. 6, pp. 765–781, 2011.

[18] A. C. Jalba, M. H. Wilkinson, and J. B. Roerdink, "Morphological hat-transform scale spaces and their use in pattern classification," *Pattern Recognition*, vol. 37, no. 5, pp. 901–915, 2004.

[19] R. C. Gonzalez, R. E. Woods, and S. L. Eddins, *Digital image processing using MATLAB*. Pearson Education India, 2004.

[20] T. F. Chan, B. Y. Sandberg, and L. A. Vese, "Active contours without edges for vector-valued images," *Journal of Visual Communication and Image Representation*, vol. 11, no. 2, pp. 130–141, 2000.

[21] K. Zhang, H. Song, and L. Zhang, "Active contours driven by local image fitting energy," *Pattern recognition*, vol. 43, no. 4, pp. 1199–1206, 2010.

[22] X. Xie, "Textured image segmentation using active contours," in *International Conference on Computer Vision, Imaging and Computer Graphics*. Springer, 2009, pp. 357–369.

[23] Q. Wu and J. An, "An active contour model based on texture distribution for extracting inhomogeneous insulators from aerial images," *IEEE Transactions on Geoscience and Remote Sensing*, vol. 52, no. 6, pp. 3613–3626, 2014.

[24] F. Ahmed, A. H. Bari, A. Shihavuddin, H. A. Al-Mamun, and P. Kwan, "A study on local binary pattern for automated weed classification using template matching and support vector machine," in *IEEE 12th International Symposium on Computational Intelligence and Informatics (CINTI)*. IEEE, 2011, pp. 329–334.

[25] P. Li, X. Lin, J. Jing, and L. Zhang, "Defect detection in fabrics using local binary patterns," in *Chinese Conference on Image and Graphics Technologies*. Springer, 2014, pp. 274–283.

[26] Z. Xia, C. Yuan, X. Sun, D. Sun, and R. Lv, "Combining wavelet transform and lbp related features for fingerprint liveness detection," *IAENG International Journal of Computer Science*, vol. 43, no. 3, pp. 290–298, 2016.

[27] F. Tajeripour, E. Kabir, and A. Sheikhi, "Fabric defect detection using modified local binary patterns," *EURASIP Journal on Advances in Signal Processing*, vol. 2008, no. 60, pp. 1–12, 2008.

[28] M. Turtinen, M. Pietikainen, and O. Silven, "Visual characterization of paper using isomap and local binary patterns," *IEICE Transactions on Information and Systems*, vol. 89, no. 7, pp. 2076–2083, 2006.

[29] B. Yang and S. Chen, "A comparative study on local binary pattern (LBP) based face recognition: LBP histogram versus LBP image," *Neurocomputing*, vol. 120, pp. 365–379, 2013.

[30] T. Ojala, M. Pietikainen, and D. Harwood, "A comparative study of texture measures with classification based on featured distributions," *Pattern recognition*, vol. 29, no. 1, pp. 51–59, 1996.

[31] M. Pietikainen, A. Hadid, G. Zhao, and T. Ahonen, *Local binary patterns for still images*. Springer, 2011.

[32] S. Taneja, C. Gupta, K. Goyal, and D. Gureja, "An enhanced k-nearest neighbor algorithm using information gain and clustering," in *Fourth International Conference on Advanced Computing and Communication Technologies (ACCT)*. IEEE, 2014, pp. 325–329.

[33] B. Sun, J. Du, and T. Gao, "Study on the improvement of k-nearest-neighbor algorithm," in *International Conference on Artificial Intelligence and Computational Intelligence, AICI'09*, vol. 4. IEEE, 2009, pp. 390–393.

[34] L. Jiang, Z. Cai, D. Wang, and S. Jiang, "Survey of improving k-nearest-neighbor for classification," in *Fourth International Conference on Fuzzy Systems and Knowledge Discovery, FSKD 2007*, vol. 1. IEEE, 2007, pp. 679–683.

[35] D. M. W. Powers, "Evaluation: from precision, recall and f-measure to roc, informedness, markedness and correlation," *Journal of Machine Learning*, vol. 2, no. 1, pp. 37–63, 2011.

[36] T. Fawcett, "An introduction to ROC analysis," *Pattern Recognition Letters*, vol. 27, no. 8, pp. 861–874, 2006.

[37] R. M. Haralick, K. Shanmugam, and I. Dinstein, "Textural features for image classification," *IEEE Transactions on Systems, Man, and Cybernetics*, vol. 3, no. 6, pp. 610–621, 1973.

[38] I. Nurtanio, E. R. Astuti, M. Hariadi, and M. H. Purnomo, "Classifying cyst and tumor lesion using support vector machine based on dental panoramic images texture features," *IAENG International Journal of Computer Science*, vol. 40, no. 1, pp. 29–37, 2013.

[39] A. M. Shabat and J.-R. Tapamo, "A comparative study of the use of local directional pattern for texture-based informal settlement classification," *Journal of Applied Research and Technology*, pp. 250–258, 2017.